Chemical Science

ROYAL SOCIETY OF CHEMISTRY

EDGE ARTICLE

View Article Online
View Journal | View Issue

Cite this: *Chem. Sci.*, 2025, **16**, 1791

All publication charges for this article have been paid for by the Royal Society of Chemistry

Controllable reconstruction of lignified biomass with molecular scissors to form carbon frameworks for highly stable Li metal batteries†

Qi Lu,‡[a] Chenyu Yang, ‡[a] Yang Xu,‡[a] Zhan Jiang,[a] Da Ke,[a] Runze Meng,[a] Sijiang Hu, [b] Yuanzhen Chen,[c] Chaofeng Zhang, [a] Jianping Yang [d] and Tengfei Zhou *[a]

Received 31st October 2024
Accepted 16th December 2024

DOI: 10.1039/d4sc07374f

rsc.li/chemical-science

Lithium metal batteries (LMBs) promise high-energy-density storage but face safety issues due to dendrite-induced lithium deposition, irreversible electrolyte consumption, and large volume changes, which hinder their practical applications. To address these issues, tuning lithium deposition by structuring a host for the lithium metal anode has been recognized as an efficient method. Herein, we report a supercritical water molecular scissor-controlled strategy to form a carbon framework derived from biomass wood. Proximate-supercritical water treatment is used to selectively cleave the β-O-4 bonds in lignin, with the extent of degradation controlled by adjusting the treatment environment's acidity. The enhanced thermal power of supercritical water molecules significantly accelerates the etching rate of lignin, increasing the porosity and permeability of the transformed carbon framework. Experimental results and multi-physics simulations show that the interconnected carbon-based pores and inner skeletal multilevel hierarchical structure facilitate rapid electron and ion transfer during battery operation and enhance electrolyte infiltration. Impressively, the as-obtained lithium metal anode exhibits long-term cycling stability for over 2000 hours at 0.5 mA cm^{-2} with low voltage overpotential. The water-treated *Pinus* (WTP)-Li//$LiCoO_2$ full cells maintain a high capacity retention rate of 93.3% and a specific capacity of 142 mA h g^{-1} at 0.5C for 100 cycles.

Introduction

Lithium metal batteries (LMBs) have garnered significant attention due to their extremely high theoretical specific capacity of 3860 mA h g^{-1} and relatively low redox potential of −3.04 V (*versus* the standard hydrogen electrode),[1–5] indicating greater potential for application in high energy density batteries. However, the use of lithium metal anodes presents several challenges.[6] First, it experiences significant volume changes during charge and discharge cycles. The uneven surface of lithium metal leads to non-uniform charge distribution, causing lithium ions to preferentially deposit in regions with higher charge density, which induces the growth of lithium dendrites.[7,8] These continuously growing dendrites can pierce the separator, causing short circuits. Additionally, the highly reactive nature of lithium metal readily leads to side reactions with the electrolyte, forming a solid electrolyte interphase (SEI) that undergoes repeated breaking and regeneration, resulting in capacity loss and increased impedance. Moreover, the high specific surface area of lithium dendrites can lead to parts detaching, which then get wrapped in the insulating SEI, forming dead lithium. This dead lithium reduces the battery's capacity and affects its cycle life.[9,10] Consequently, the direct use of lithium metal anodes may result in low cycle performance and thermal runaway risks, significantly hindering the commercialization of LMBs.[11]

In order to solve the multiple existing problems mentioned above, numerous studies have been conducted by researchers.[12–14] Introducing Li metal into a host is a promising strategy for stabilizing Li metal anodes.[15] Cui *et al.* introduced the concept of a scaffold/host strategy to mitigate volume changes, and reported a layered Li-reduced graphene oxide composite anode by the melting-diffusion method.[16] Lu *et al.* developed a facile strategy to simultaneously KOH-etch and nitrogen-dope commercial carbon cloth into a 3D

[a]*Institutes of Physical Science and Information Technology, Key Laboratory of Structure and Functional Regulation of Hybrid Material (Ministry of Education), Anhui University, Hefei 230601, China. E-mail: tengfeiz@ahu.edu.cn*

[b]*Guangxi Key Laboratory of Low Carbon Energy Material, Guangxi Normal University, Guilin, 541004, China*

[c]*The State Key Laboratory for Mechanical Behavior of Materials, School of Materials Science and Engineering, Xi'an Jiaotong University, Xi'an 710049, P. R. China*

[d]*State Key Laboratory for Modification of Chemical Fibers and Polymer Materials, College of Materials Science and Engineering, Donghua University, Shanghai 201620, China*

† Electronic supplementary information (ESI) available. See DOI: https://doi.org/10.1039/d4sc07374f

‡ Q. L., C. Y. and Y. X. contributed equally to this work.

multifunctional host anode for LMBs.[17] Eom *et al.* focused on the lithiophobic behaviors of metals caused by crystallographic discrepancies and the feasibility of using Ti metals as shields to block the electrodeposition of Li on the top surface of the 3D-host. While the structural design methods of lithium metal hosts have somewhat improved the cycling performance of lithium batteries, they still cannot entirely prevent the formation of dead lithium and anode volume expansion.[18–20] The coulombic efficiency remains suboptimal, and the high cost and complex preparation of the scaffolds continue to impede their practical application.

Carbon frameworks derived from biomass wood stand out due to their low cost, wide availability, renewability, and environmental friendliness. These frameworks retain the inherent chamber structure of the original cytoderm, which, when used as a substrate for lithium metal battery anodes, directs the uniform deposition of lithium metal in designated spaces and accommodates its expansion and contraction during charge–discharge cycles.[21,22] Additionally, the interconnected carbon-based pores facilitate rapid electron and ion transfer during battery operation and enhance electrolyte infiltration. For instance, Wu's group prepared self-supporting hyphae carbon nanobelts as hosts by carbonizing hyphae balls of Rhizopus.[23] However, directly carbonized biomass anodes lack refined surface structures, limiting their lithium affinity, electrolyte wettability, and long-term structural stability, thereby constraining their application in high-performance lithium metal batteries.[24–26] Therefore, there is an urgent need to use pretreatment methods to modify the surface structure, porosity, and permeability of these anodes.

To explore the effect of applying biomass carbon with different microstructures on LMB cycling performance, this study utilized *Pinus sylvestris* as the biomass wood. The primary components of pine wood cell walls are hemicellulose (20–30 wt%), cellulose (40–50 wt%), and lignin (10–35 wt%).[27] Hemicellulose and cellulose are polymers of C5 and C6 sugars with specific ether bonds, whereas lignin is a more complex, three-dimensional, amorphous polymer composed of various phenolic monomers connected by ether and carbon–carbon bonds.[28–30] Moreover, lignin, being the backbone of wood, can be selectively degraded by breaking part of its valence bond structure to achieve the desired carbon framework that can be carbonized after modification.[31,32] In this study, supercritical water treatment is used to selectively cleave the β-O-4 bonds in lignin, effectively degrading and transforming the biomass wood. The depth and extent of degradation can be precisely controlled by adjusting the acidity. After carbonization, the undegraded lignin matrix exhibits a three-dimensional fine structure with a rigid, multi-level surface architecture.[33] This microstructure facilitates the uniform deposition of molten lithium metal and enhances the absorption and infiltration of the electrolyte, providing sufficient space to accommodate volume changes during electrochemical processes. When applied to LMBs, water-treated *Pinus* (WTP)-Li symmetric cells can cycle stably for over 2000 hours at a high current density with low overpotential. Additionally, when paired with lithium cobalt oxide ($LiCoO_2$) as the cathode in full cells, performance is significantly improved. This study offers new options for three-dimensional LMB host materials and proposes innovative approaches for their practical application.

Results and discussion

Scheme 1 illustrates the formation process of carbon frameworks derived from biomass wood. Lignin, a major component, forms the core of the cell walls of plants alongside cellulose, while hemicellulose binds these polymers together. Proximate-supercritical water treatment of biomass wood in different acidic environments breaks down bonds in lignin, cellulose, and hemicellulose, which are then carbonized to form biomass carbon.[34] These carbon frameworks retain the three-dimensional, uniform porous structure of pine while exhibiting a certain rigidity. To further verify the cleavage of lignin and other substances, gas chromatography-mass spectrometry (GC-MS) analysis was conducted on the liquids after hydrothermal reactions of proximate-supercritical WTP, base-treated *Pinus* (BTP), and acid-treated *Pinus* (ATP). The data in Scheme 1 indicate that the cleavage of lignin in WTP produces a substantial amount of guaiacol monomers, along with small amounts of acids and phenols. BTP contains a minor amount of guaiacol monomers and acids, mostly aldehydes and ketones. In ATP, only trace amounts of aldehydes and ketones are present, further confirming the bond cleavage positions shown in Scheme 1. During proximate-supercritical water treatment, under supercritical conditions, water is likely to exist in monomeric or dimeric states owing to a substantial decrease in hydrogen-bond content. This reduction in both the hydrogen bond count and the dielectric constant allows supercritical water to function as a low-polarity solvent, capable of achieving complete miscibility with small-molecule organics and gases. Consequently, a homogeneous reaction environment is established.[35,36] The homologous OH^- ions in water molecules selectively break the β-O-4 bonds in lignin without cleaving the C–C bonds, forming guaiacol monomers. H^+ ions generate single phenolic substances such as aromatic hydrocarbons and phenols, and they hydrolyze cellulose and hemicellulose into acids, resulting in a three-dimensional carbon skeleton with a multi-layer foam carbon structure. However, during alkaline treatment, the yield of guaiacol monomers is less than 10%, due to the attack of OH^- ions on a significant number of lignin monomers, leading to the formation of derivatives such as aromatics and ketones. Conversely, in acidic treatment, minimal disruption of the bonds within lignin and other substances occurs, thereby preserving the three-dimensional structure of the wood (Scheme 1).

After the preparation of the hierarchical structure of the carbon frameworks, we compared it with copper foam, nickel foam, carbon paper, and carbon cloth as lithium host materials. Scanning electron microscopy (SEM) depicted different lithium 3D carrier materials, all exhibiting 3D disordered structural topography, while biomass carbon was uniformly porous (Fig. S1†). The cross-sectional SEM image (Fig. S1e†) reveals numerous micro-sized pores of varying diameters that act as crucial channels for lithium electrodeposition and stripping.

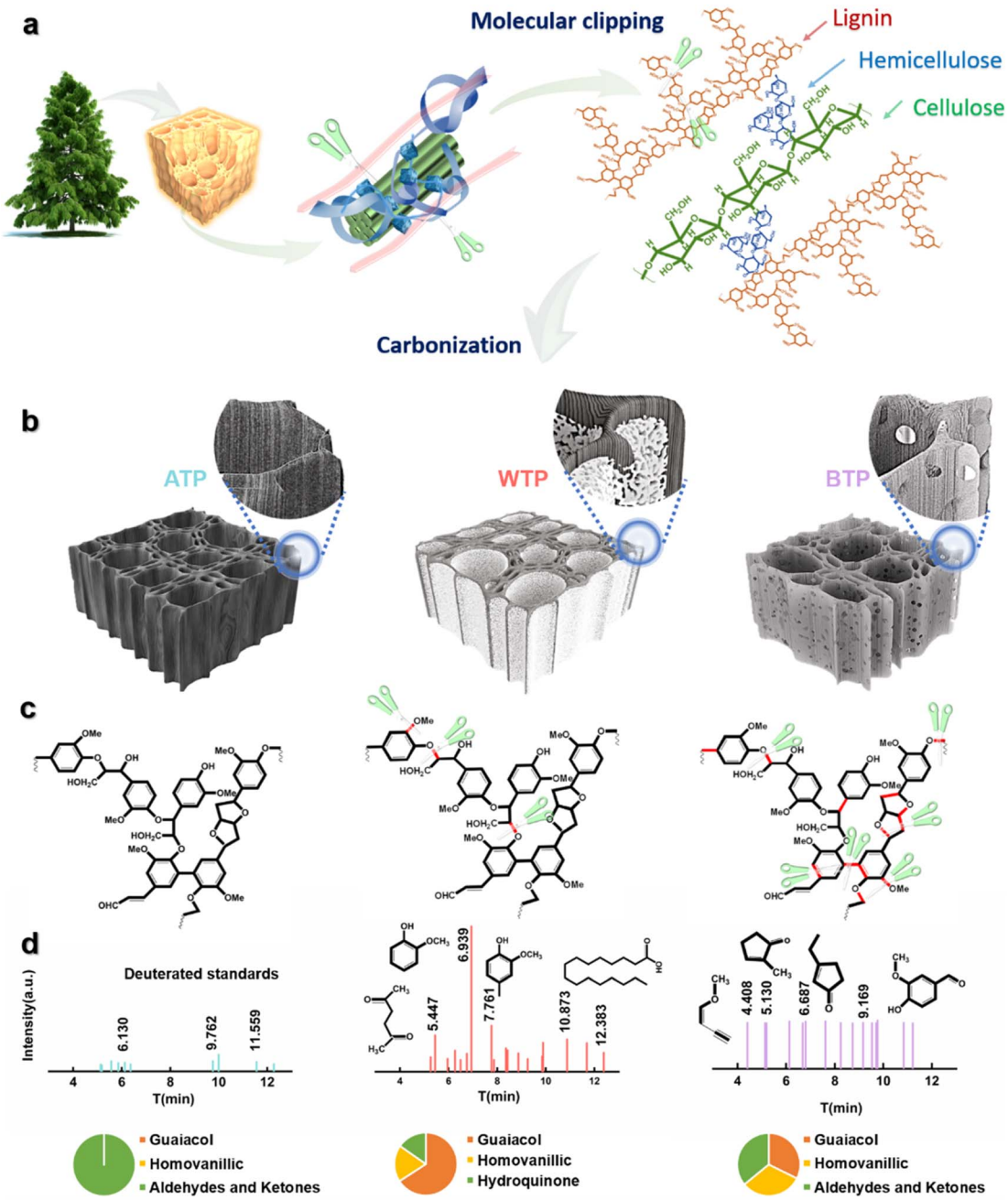

Scheme 1 The formation process of carbon frameworks derived from biomass wood and the bond cleavage of lignin in wood. (a and b) Schematic illustration of the fabrication and the structures of ATP, WTP and BTP. (c) Cleavage location of lignin bonds in ATP, WTP and BTP. (d) GC-MS analysis of the solution after the hydrothermal reaction of ATP, WTP and BTP (pie chart illustrates the content of the pyrolysis product).

Meanwhile, the longitudinal SEM image (Fig. S1f†) demonstrates that the wood possesses vertically aligned, low-curvature channels that expedite electrolyte transmission and promote swift migration of lithium ions, thus significantly improving the battery's cycling stability. By adjusting the treatment environment's acidity, we achieved a wide range of surface microstructure morphologies. We investigated the effects of different surface microstructures of biomass carbon as a host of lithium in LMBs. The carbonized biomass after proximate-supercritical water treatment exhibits a multi-level structure, with a dense inner carbon skeleton and a foam-like porous outer layer (Fig. 1a and b).[37] Fig. 1c shows a high-resolution transmission electron microscopy (HRTEM) image of a WTP sample. The carbon skeleton structure of BTP is extensively destroyed and penetrated by alkalis, forming micro-surfaces with a large number of irregular pores (Fig. 1d). In contrast, the biomass carbon treated with acid and directly carbonized without any treatment demonstrates both intact inner and outer carbon skeleton structures (Fig. 1e and f).

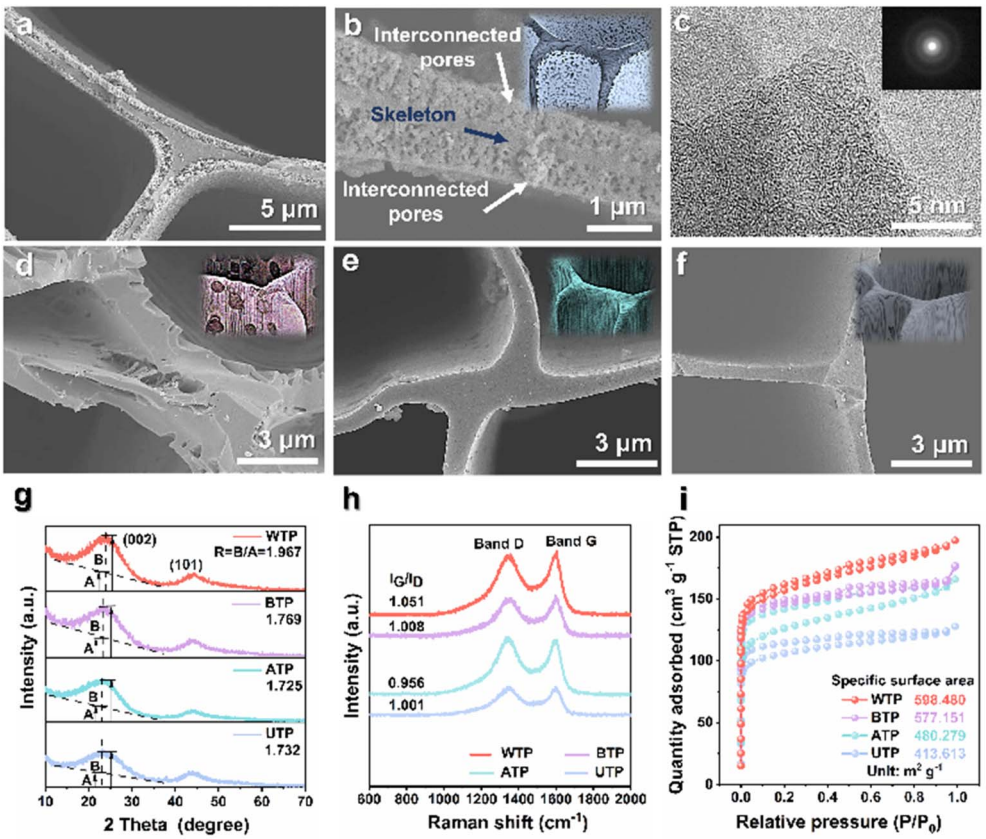

Fig. 1 Characterization of the graphitization and morphology of carbon materials. SEM images of (a and b) WTP, (d) BTP, (e) ATP and (f) UTP. (c) HRTEM image of WTP. (g) XRD patterns, (h) Raman spectra and (i) N_2 adsorption/desorption curves of WTP, ATP, BTP and UTP.

X-ray diffraction (XRD) was used to further characterize the carbon crystal structure and graphitization. The presence of two distinct characteristic peaks (002) and (101) in Fig. 1g corresponds to the amorphous structure and the degree of graphitization of the carbonized wood, respectively. The graphitization degree of various biomass carbons was compared by calculating their corresponding *R*-values.[38,39] The *R*-value of the WTP sample was 1.967, which was higher than the *R*-values of the BTP (1.769), the ATP (1.725), and the untreated *Pinus* (UTP) sample (1.732). This suggests that the WTP sample exhibits a superior degree of crystallinity and higher electrical conductivity, thereby facilitating electron transfer and Li^+ transport.[40] Furthermore, the various biomass carbons were characterized using Raman spectroscopy. The D band, located at 1350 cm^{-1}, corresponds to the defects and amorphous carbon structure of the carbon material. The G band is situated at 1580 cm^{-1}, corresponding to the in-plane vibrations caused by graphite (Fig. 1h).[41] The Raman spectrum's G/D intensity ratio (I_G/I_D) indicates the degree of graphitization, with a higher ratio indicating better crystallinity and superior electrical conductivity.[42] This indicates that WTP has a higher degree of graphitization, followed by BTP, while the degree of graphitization of ATP is comparatively poorer than that of UTP.[43] N_2 adsorption–desorption experiments can demonstrate the specific surface area and pore size distribution of different biomass carbons. The adsorption and desorption curves of biomass carbon for nitrogen belong to the typical type I adsorption. There is a rapid increase in adsorption at lower relative pressures, and the adsorption appears to be saturated at a certain relative pressure.[44] This reflects the presence of a pronounced microporous structure (Fig. 1i). WTP has the largest specific surface area of 598.480 m^2 g^{-1} and a smaller average pore size of 3.825 nm. This provides an advantage over the other samples as it can provide a large number of active sites and buffer locations for lithium metal plating and stripping, thus improving the cycling stability of the battery (Fig. S2†).

In view of the deposition behavior of lithium metal on various three-dimensional materials, we used SEM to study the morphological deposition of lithium metal at a current density of 1.0 mA cm^{-2} under different plating times. First, we compared the lithium deposition behavior on copper foam, nickel foam, carbon paper, and carbon cloth (Fig. S3†). Lithium metal deposits unevenly on the surfaces of these three-dimensional hosts. As the lithium plating time increases, a substantial amount of inactive lithium and even dead lithium accumulates on the host surfaces, leading to the formation of numerous lithium dendrites. In comparison to three-dimensional hosts like copper foam, metallic lithium deposits more uniformly on biomass carbon.[45] The numerous pores in biomass carbon provide a significant number of deposition

channels for metallic lithium. Particularly in WTP, lithium metal tends to nucleate and grow primarily on the outer layer of carbon foam before gradually extending into the vertical channels and ultimately filling the entire channel (Fig. 2d). COMSOL Multiphysics simulations were performed on the lithium deposition behavior in WTP and UTP. As shown in the simulation results, the unique multi-level carbon structure of WTP is able to guide lithium deposition on the pore surface, indicating that lithium dendrite growth and electrode volume changes are successfully regulated by the 3D carbon skeleton structure. However, a large amount of lithium in UTP gradually accumulates at the bottleneck over time, eventually leading to dendrite formation (Fig. 2f). Meanwhile, during lithium deposition, a considerable amount of metallic lithium tends to nucleate and accumulate on the surface of biomass carbon in both ATP and UTP (Fig. 2b and c), which can lead to channel blockage and wastage of space volume. Upon comparison, it has been found that proximate-supercritical water treatment plays a significant role in the processing of biomass carbon, particularly in guiding the nucleation and deposition process of lithium metal. This multi-level structure exhibits improved lithium ion transport kinetics.[46,47] After 20 cycles, we disassembled and removed the lithium composite carbon sheets and reacted them with water and ethanol. The results showed that the original structure and morphology of WTP-Li was unchanged after reacting with both water and ethanol, whereas BTP-Li, ATP-Li, and UTP-Li were completely shattered after the reaction (Fig. 2g). The rigid inner surface carbon skeleton of proximate-supercritical water-treated WTP samples ensures complete preservation of the naturally occurring pore structure of the carbon material. Simultaneously, the high toughness foam-like outer surface carbon can significantly accommodate volume strain. This multi-level structure promotes the formation of a stable SEI during lithium metal plating/stripping processes, thereby maintaining the structural integrity of WTP.[48] At a current density of 1 mA cm^{-2} and a capacity of 1 mA h cm^{-2}, the nucleation behavior of lithium during the first cycle of deposition shows a gradually increasing curve, eventually reaching a plateau. This plateau represents the polarization voltage (Fig. 2e).[49,50] The nucleation overpotential of the WTP electrode is the lowest at −28 mV, while the BTP electrode, ATP electrode, UTP electrode, and bare Li electrode have poor lithium affinity, resulting in their nucleation overpotentials being −75 mV, −139 mV, −161 mV, and −186 mV, respectively. The WTP electrode exhibits a lower nucleation overpotential, further demonstrating the effective reduction of impedance in battery cycling by the multi-level

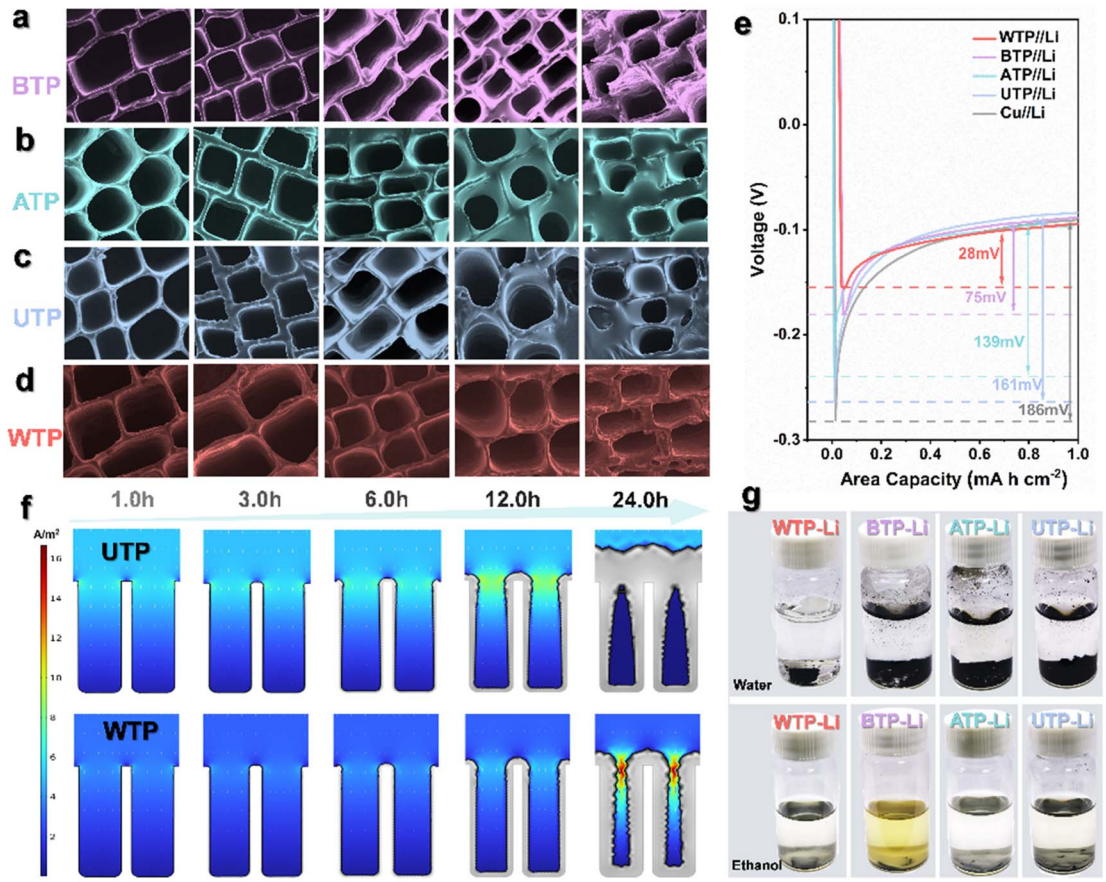

Fig. 2 Lithium deposition and structural stability of different carbon materials. The SEM images of (a) BTP, (b) ATP, (c) UTP and (d) WTP after plating 1.0 h, 3.0 h, 6.0 h, 12.0 h and 24.0 h lithium at 1.0 mA cm^{-2}, respectively (scale bar is 20 μm). (e) Voltage–capacity curve of lithium deposition nucleation. (f) Simulation results of lithium deposition behavior in the WTP cathode. Here, the arrows represent the electrolyte current density vector. (g) Reaction diagram of WTP-Li, BTP-Li, ATP-Li, and UTP-Li with deionized water and anhydrous ethanol.

structured carbon for water treatment. This also demonstrates superior ion/electron transport capabilities.[51]

Molten lithium impregnation experiments were conducted on directly carbonized UTP and WTP to study the wettability of biomass carbon and molten lithium, influenced by different surface microstructures. The results demonstrate that molten metallic lithium can completely and uniformly penetrate WTP samples within 12 seconds, in contrast to the slower diffusion and uneven distribution observed in UTP samples (Fig. 3a and c). Additionally, the integration of biomass carbon with lithium metal significantly enhances ductility, thereby facilitating the assembly of subsequent battery components. Meanwhile, the wetting behavior of molten lithium metal was simulated (Fig. 3b and d). This demonstrates the good lithium affinity and strong capillary action of WTP biomass carbon. To investigate the electrochemical reaction kinetics of metallic lithium under WTP modification, electrochemical impedance spectroscopy (EIS) tests were performed on symmetric cells composed of

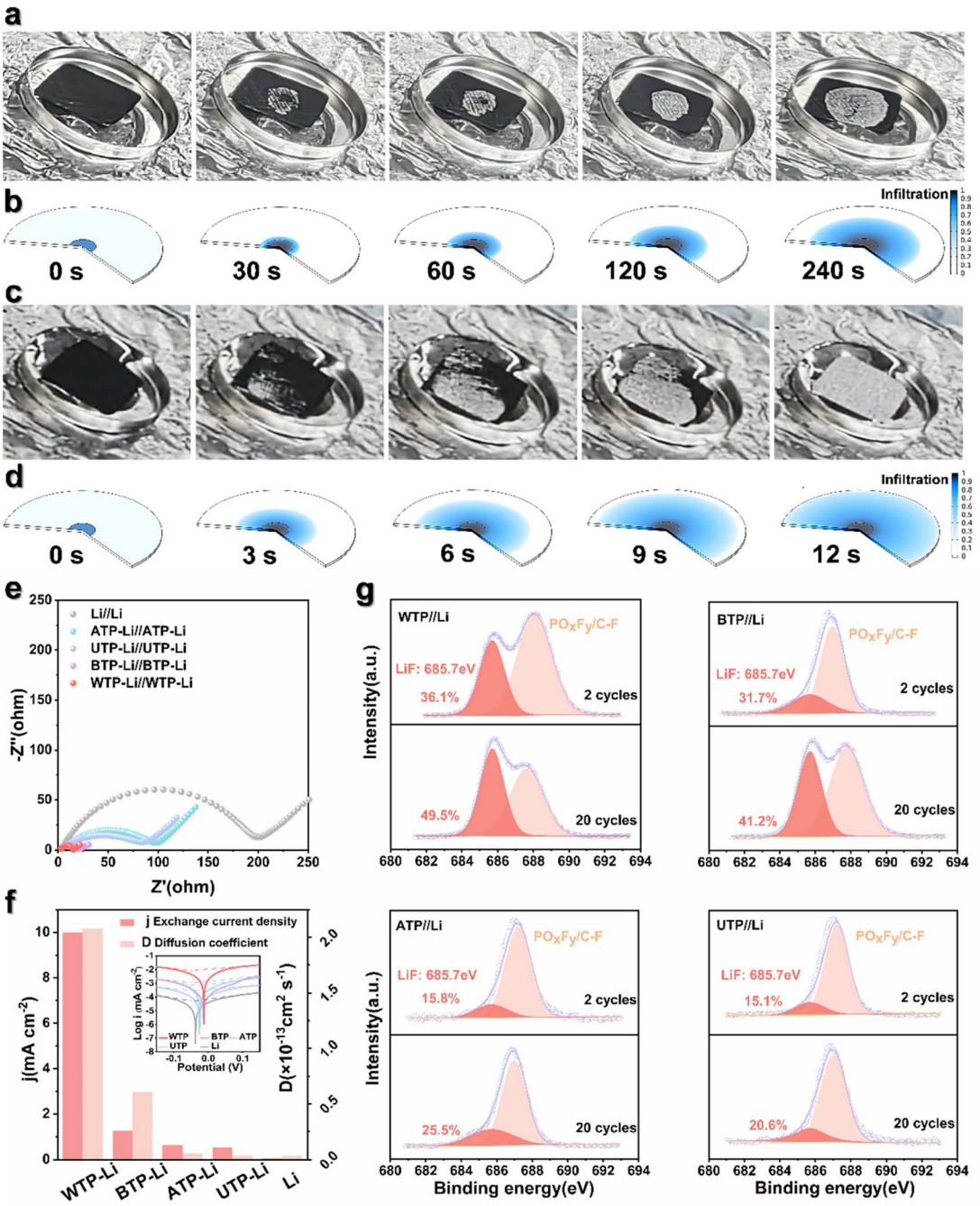

Fig. 3 Reaction kinetics of lithium in different carbon materials. Infiltration of (a) WTP and (c) UTP with molten lithium. Molten lithium infiltration simulations corresponding to (b) WTP and (d) UTP. (e) After 50 cycles, EIS of the WTP-Li electrode, BTP-Li electrode, ATP-Li electrode, UTP-Li electrode and bare lithium electrode. (f) Exchange current density and lithium ion diffusion coefficient statistical histogram. (g) XPS spectra of WTP-Li, BTP-Li, ATP-Li and UTP-Li electrode F 1s.

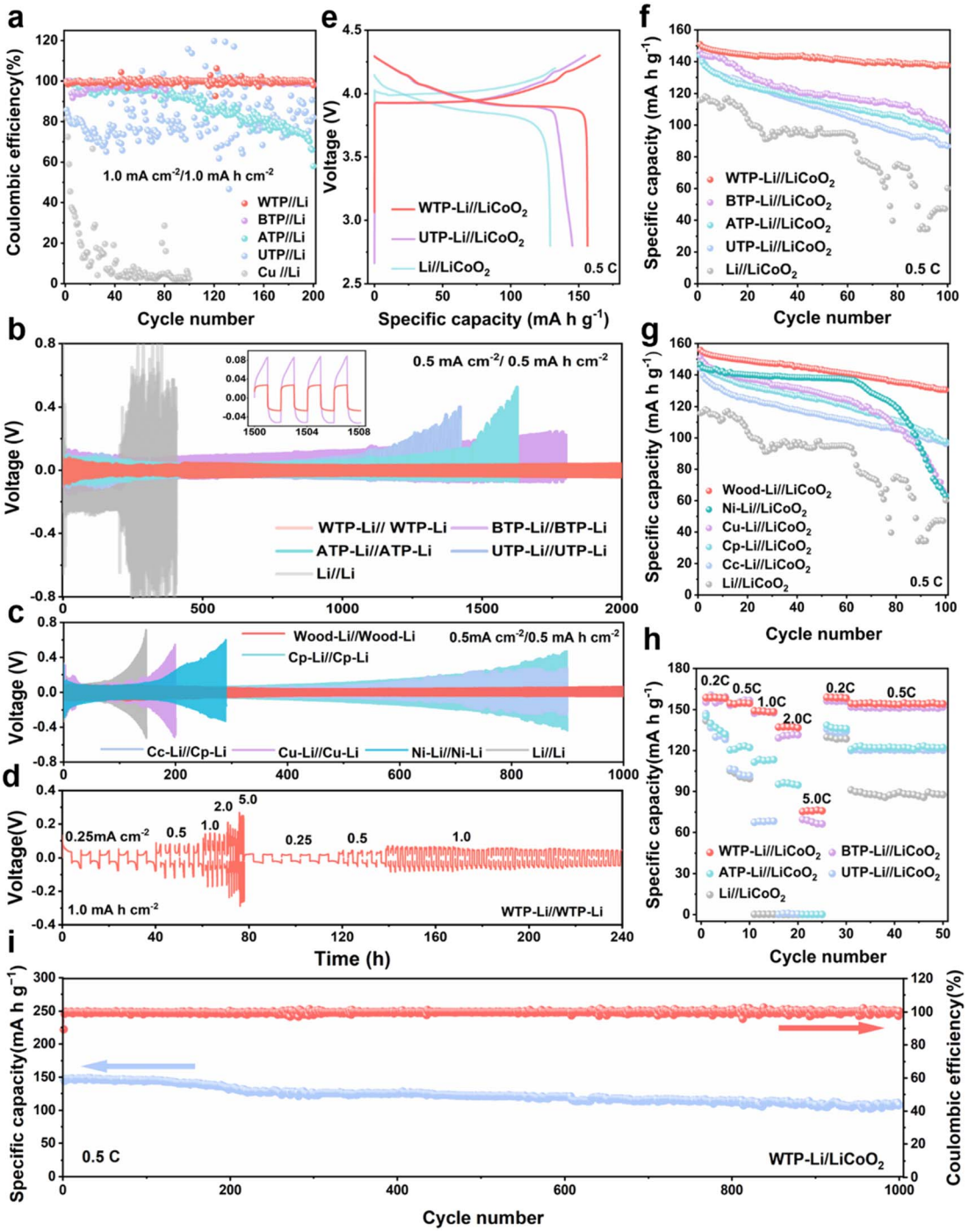

Fig. 4 Electrochemical properties of various lithium metal anodes. (a) Coulombic efficiencies (CEs) of different biologically derived, carbon-based lithium electrodes at a current density of 1.0 mA cm^{-2}. (b) Voltage-time profiles of lithium stripping/plating cycles for WTP-Li, BTP-Li, ATP-Li, UTP-Li, and Li foil electrodes in symmetric cells at a current density of 0.5 mA cm^{-2} and a capacity of 0.5 mA h cm^{-2}. (c) Voltage-time profiles of lithium stripping/plating cycles for various lithium three-dimensional composite electrodes in symmetric cells at a current density of 0.5 mA cm^{-2} and a capacity of 0.5 mA h cm^{-2}. (d) Rate performance of WTP-Li symmetric cells at current densities ranging from 0.25 to 5.0 mA cm^{-2}, with a stripping/plating capacity of 1.0 mA h cm^{-2}. (e) Initial charge and discharge curves for WTP-Li, UTP-Li, and bare lithium full batteries assembled with different biologically derived, carbon-based lithium electrodes. (f) Cycling performance of full cells. (g) Cycling performance of symmetric cells with various lithium three-dimensional composite electrodes. (h) Rate performance of full cells. (i) Cycling performance at 0.5C (where 1C = 140 mA h g^{-1}).

WTP-Li/WTP-Li, BTP-Li/BTP-Li, ATP-Li/ATP-Li, UTP-Li/UTP-Li, and Li/Li. The symmetric cells were cycled at a current density of 1 mA cm^{-2} for one hour per charge/discharge cycle. Prior to cycling, the R_{ct} value of the WTP-Li electrode was 17.82 Ω, which is lower than that of the BTP-Li, ATP-Li, UTP-Li, and bare Li electrodes (Fig. S3†). After 50 cycles, the R_{ct} value of the WTP-Li

electrode decreased to 11.63 Ω, remaining lower than that of the other four electrodes (Fig. 3e). The impedance spectrum from EIS indicates a lower impedance during the reaction process of the WTP-Li electrode, confirming that the multi-level structured carbon formed by water treatment effectively reduces interfacial resistance, thereby facilitating faster charge transfer kinetics and Li^+ transport capability. Additionally, the Warburg factor (σ) related to Li^+ diffusion in the low-frequency region was calculated by determining the slope of Z' *versus* $\omega^{-1/2}$ ($Z' \propto \sigma\omega^{-1/2}$). The diffusion coefficient of lithium ions (D value) was determined using the empirical equation $D = 0.5\ (R^2T^2/A^2n^4F^4C^2\sigma^2)$.[52] After 50 cycles, the Li^+ diffusion coefficient of the WTP-Li electrode was 2.08×10^{-13} $cm^2\ s^{-1}$, which is higher than that of the BTP-Li (6.09×10^{-14} $cm^2\ s^{-1}$), ATP-Li (5.68×10^{-15} $cm^2\ s^{-1}$), UTP-Li (3.62×10^{-15} $cm^2\ s^{-1}$), and bare Li electrodes (3.48×10^{-15} $cm^2\ s^{-1}$) (Fig. S5†). This result further demonstrates faster ion/electron transfer kinetics in WTP electrodes. Tafel curve tests were also conducted on symmetric cells of WTP-Li/WTP-Li, BTP-Li/BTP-Li, ATP-Li/ATP-Li, UTP-Li/UTP-Li, and Li/Li (Fig. S6†) to calculate the exchange current density of each electrode.

To further understand the reaction kinetics of lithium metal under WTP electrodes and the degree of electrode polarization corrosion, we summarize the exchange current density and Li^+ diffusion coefficient in four carbon framework electrodes and Li/Li symmetrical batteries.[53] The exchange current density (j value) of the WTP-Li electrode is 9.98 mA cm^{-2}, which is higher than that of BTP-Li (1.25 mA cm^{-2}), ATP-Li (0.62 mA cm^{-2}), UTP-Li (0.53 mA cm^{-2}), and bare lithium (0.06 mA cm^{-2}) (Fig. 3f). The higher exchange current density indicates superior

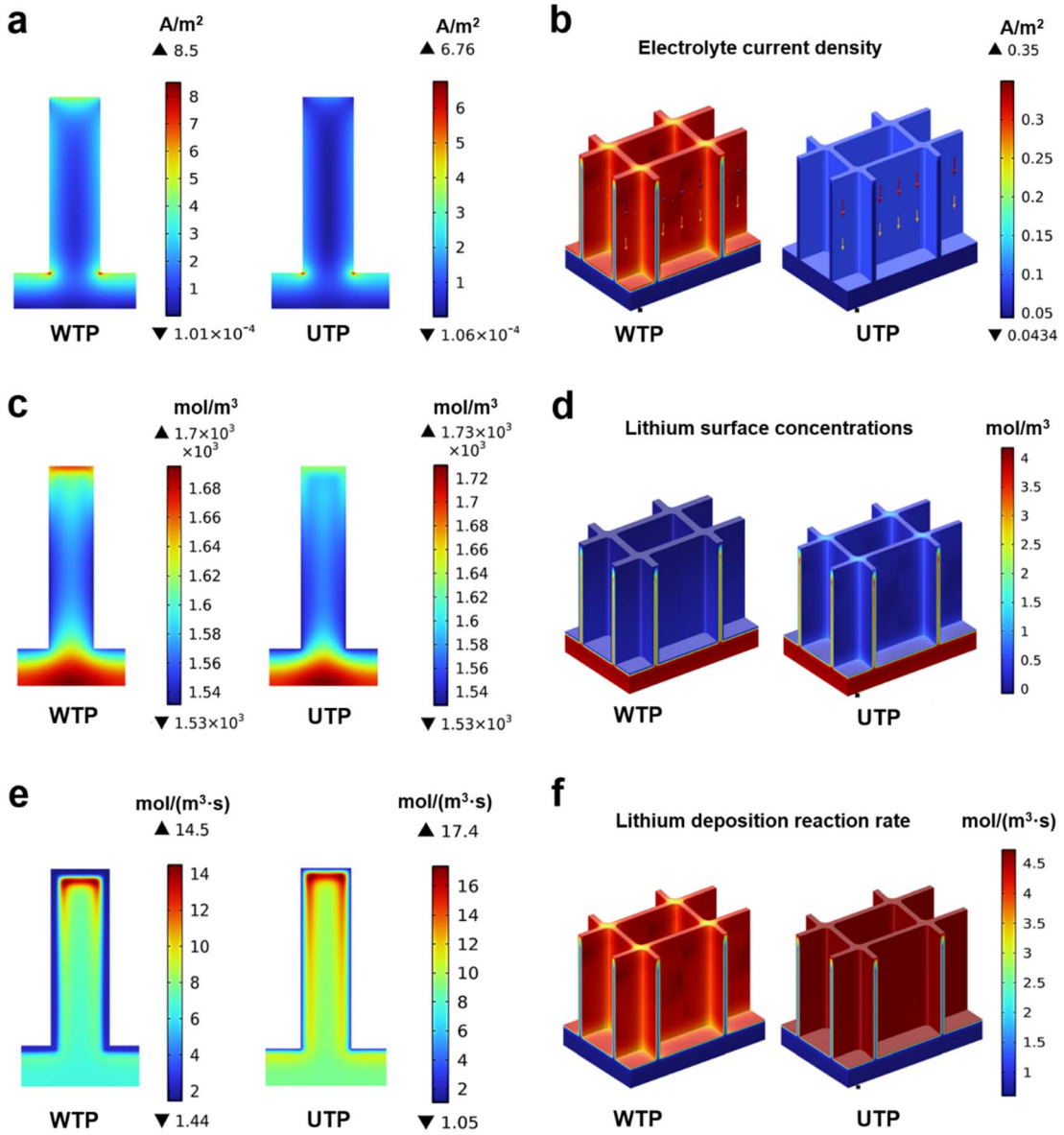

Fig. 5 2D and 3D COMSOL Multiphysics simulations of WTP and UTP electrodes. (a and b) Simulation results of the electrolyte current density of the WTP anode and UTP anode. (c and d) Simulation results of lithium surface concentrations. (e and f) Simulation results of the reaction rate of lithium deposition.

charge transfer kinetics and Li^+ transport capability, which is consistent with the EIS analysis results. LiF is an important component of the SEI membrane. Studies have shown that the protective effect of lithium fluoride on the cathode is due to its rapid lithium ion conduction mechanism. Furthermore, lithium fluoride has high surface energy and a low Li^+ diffusion barrier, which promotes uniform deposition of Li^+.[54] X-ray photoelectron spectroscopy (XPS) was used to analyze the composition of LiF in the SEI on the surface of electrodes after 2 and 20 cycles in a half-cell. The percentage of LiF in the WTP electrode is higher after 2 cycles (36.1%) and 20 cycles (49.5%) compared to other electrodes (Fig. 3g). These results indicate that, compared with ATP, BTP, and UTP, the WTP multi-level carbon foam skeleton can generate more active lithium than dead lithium during battery cycling, exhibiting better lithium-ion transport kinetics and charge transfer capabilities. At a current density of 1 mA cm^{-2}, the coulombic efficiency (CE) of BTP and ATP began to decay after 100 cycles and dropped to 60% after 200 cycles. The CE of the UTP electrode oscillated at around 70% during cycling. In contrast, the WTP electrode maintained a CE of 99% even after 200 cycles (Fig. 4a), indicating excellent CE primarily due to its unique multilevel carbon structure, which enhances lithium deposition/stripping behavior.[55] We assembled symmetric cells and found that the WTP-Li electrode had the lowest overpotential of around 56 mV after 2000 hours of cycling (Fig. 4b). This superior cycling stability is attributed to the multilevel carbon structure of the WTP-Li electrode.

After 300 hours of cycling, the overpotential of copper foam, nickel foam, and bare lithium electrodes exceeded 500 mV at a current density of 0.5 mA cm^{-2}. Similarly, the carbon paper and carbon cloth electrodes exhibited overpotentials far exceeding 500 mV after 900 hours of cycling. In contrast, the hierarchical carbon framework lithium electrode maintained an overpotential of approximately 80 mV even after 1000 hours of cycling, and only the carbon framework electrode maintained a CE above 90% after 200 cycles (Fig. 4c and g). This demonstrates the superior cycling stability of carbon framework lithium electrodes compared to other composite electrodes.[56] We also evaluated the rate performance of the WTP-Li electrode in symmetric cells. With a cycling capacity of 1 mA h cm^{-2}, the polarization voltage of the WTP-Li electrode remained approximately 240 mV as the current density increased from 0.25 to 5.0 mA cm^{-2}. When the current density was subsequently reduced, the polarization voltage stabilized at around 60 mV (Fig. 4d). This performance can be attributed to the abundant porous 3D channels of WTP, which mitigate lithium deposition-induced volume strain, and the foamy outer carbon structure that guides uniform lithium deposition.[57] Fig. 4e compares the initial cycle charge/discharge curves of WTP-Li, UTP-Li, and bare lithium full cells, revealing a higher initial charge/discharge capacity for the WTP-Li full cell. After 100 cycles, the WTP-Li//$LiCoO_2$ cell demonstrated the highest capacity retention rate of 93.3% (Fig. 4f).

Rate performance tests on full cells further showed that the WTP-Li full cell maintained a high and stable specific capacity (Fig. 4h). The high capacity retention rate and excellent overall cell kinetics of the WTP electrode make it suitable for practical battery applications.[58–61] At 0.5C, the WTP-Li//$LiCoO_2$ cell achieved a discharge capacity of 108.07 mA h g^{-1} after 1000 cycles, with coulombic efficiencies exceeding 73.54% (Fig. 4i). These results, from both symmetric and full cell perspectives, demonstrate that WTP as a 3D host exhibits outstanding electrochemical performance, characterized by a stable SEI, rapid ion/electron transport capability, and uniform dendrite-free lithium deposition. To demonstrate the superiority of the hierarchical carbon framework structure of WTP in terms of lithiphilicity, we created 2D and 3D models of WTP and UTP to model the Li deposition behavior using the COMSOL Multiphysics simulations. The simulation results reveal a more uniform distribution of electrolyte current density within the WTP electrode (Fig. 5a and b). Additionally, high lithium ion concentration points are evenly dispersed at the bottom of the WTP channel and at the layer's edge, resulting in the deposition of lithium on the surface of the carbon skeleton (Fig. 5c and d). At the same time, the dissolution–deposition reaction rate of lithium on the WTP electrode is significantly faster than that of UTP (Fig. 5e and f), which indicates that dead lithium is easy to be generated on UTP. During the charge/discharge cycles, the severe accumulation of dead lithium can result in decreased CE and poor cycling stability.

Conclusions

The β-O-4 bond in lignin was selectively controlled and cleaved using a proximate-supercritical water treatment method, resulting in a WTP sample with a dense inner carbon skeleton and an external porous foam structure after carbonization. The WTP samples not only preserve the three-dimensional skeletal structure of the wood but also possess natural porosity and defects that enable uniform lithium deposition on their surface and retention of more active lithium. Specifically, experimental results and multi-physics simulations indicated that WTP samples with multi-level surface structures can significantly reduce the local current density at the anode, thereby delaying the initial nucleation of lithium dendrites. This technique restricts lithium expansion within the pores and mitigates the volume increase caused by metallic lithium during charge–discharge cycles. Consequently, at a current density of 0.5 mA cm^{-2} and a cycling capacity of 0.5 mA h cm^{-2}, the symmetrical battery can cycle stably for over 2000 hours while maintaining a low overpotential. Additionally, when paired with a $LiCoO_2$ cathode, the full cell exhibits a high capacity retention rate of 93.3% after stable cycling for 100 cycles at a current density of 0.5C, maintaining a specific capacity of 142 mA h g^{-1} Moreover, the biomass carbon with a surface microstructure obtained has potential for application in high-energy-density all-solid-state lithium batteries and lithium–carbon dioxide, lithium–oxygen, and lithium–sulfur batteries, providing significant references for the application of biomass.

Data availability

The data supporting this article have been included as part of the ESI.†

Author contributions

Q. L., C. Y. and Y. X. contributed equally to this work. Q. L. performed writing of the original draft and formal analysis; C. Y. supported review, editing and investigation; Y. X. performed data formal analysis and investigation; Z. J. and D. K. contributed to creating the images; R. M. supported data curation; S. H., Y. C., C. Z., J. Y. and T. Z. conceived the project, and provided guidance and supervision throughout the work.

Conflicts of interest

There are no conflicts to declare.

Acknowledgements

This work was supported by the Anhui Provincial Natural Science Foundation for Outstanding Young Scholar (2208085Y05), the Anhui Provincial Scientific Reuter Foundation for Returned Scholars (2022LCX030), the National Natural Science Foundation of China (52172173), the Excellent Research and Innovation Team Project of Anhui Province (2022AH010001) and Guangxi Key Laboratory of Low Carbon Energy Material (2021GXKLLCEM04).

Notes and references

1 Y. Cao, M. Li, J. Lu, J. Liu and K. Amine, *Nat. Nanotechnol.*, 2019, **14**, 200.
2 J. Liu, Z. Bao, Y. Cui, E. J. Dufek, J. B. Goodenough, P. Khalifah, Q. Li, B. Y. Liaw, P. Liu and A. Manthiram, *Nat. Energy*, 2019, **4**, 180.
3 J. Xiao, Q. Li, Y. Bi, M. Cai, B. Dunn, T. Glossmann, J. Liu, T. Osaka, R. Sugiura and B. Wu, *Nat. Energy*, 2020, **5**, 561.
4 J. Li, Z. Kong, X. Liu, B. Zheng, Q. H. Fan, E. Garratt, T. Schuelke, K. Wang, H. Xu and H. Jin, *InfoMat*, 2021, **3**, 1333.
5 C. Yang, Z. Jiang, X. Chen, W. Luo, T. Zhou and J. Yang, *Chem. Commun.*, 2024, **60**, 10245–10264.
6 C. Zhu, C. Sun, R. Li, S. Weng, L. Fan, X. Wang, L. Chen, M. Noked and X. Fan, *ACS Energy Lett.*, 2022, **7**, 1338.
7 X. Wang, Z. Chen, K. Jiang, M. Chen and S. Passerini, *Adv. Energy Mater.*, 2024, **14**, 2304229.
8 Y. Zhang, M. Yao, T. Wang, H. Wu and Y. Zhang, *Angew. Chem., Int. Ed.*, 2024, **63**, e202403399.
9 Z. Li, Z. Chen, N. Sun, D. Wang, X. Yao and Z. Peng, *Angew. Chem., Int. Ed.*, 2024, **136**, e202400876.
10 X. Xu, Q. Jiang, C. Yang, J. Ruan, W. Zhao, H. Wang, X. Lu, Z. Li, Y. Chen, C. Zhang, J. Hu and T. Zhou, *Chem. Sci.*, 2024, **15**, 3262–3272.
11 N. Zhang, T. Deng, S. Zhang, C. Wang, L. Chen, C. Wang and X. Fan, *Adv. Mater.*, 2022, **34**, 2107899.
12 M. Niu, L. Dong, J. Yue, Y. Li, Y. Dong, S. Cheng, S. Lv, Y. Zhu, Z. Lei, Y. Liang, S. Xin, C. Yang and Y. Guo, *Angew. Chem., Int. Ed.*, 2024, **63**, e202318663.
13 S. Chen, J. Zhang, L. Nie, X. Hu, Y. Huang, Y. Yu and W. Liu, *Adv. Mater.*, 2021, **33**, 2002325.
14 J. Jiang, Y. Ou, S. Lu, C. Shen, B. Li, X. Liu, Y. Jiang, B. Zhao and J. Zhang, *Energy Storage Mater.*, 2022, **50**, 810.
15 S. Park, H. J. Jin and Y. S. Yun, *Adv. Mater.*, 2020, **32**, 2002193.
16 D. Lin, Y. Liu, Z. Liang, H.-W. Lee, J. Sun, H. Wang, K. Yan, J. Xie and Y. Cui, *Nat. Nanotechnol.*, 2016, **11**, 626.
17 F. Cheng, X. Yang, O. Ka, L. Wen, X. Wang and W. Lu, *J. Mater. Chem. A*, 2023, **11**, 4205.
18 D. Lin, Y. Liu, Y. Li, Y. Li, A. Pei, J. Xie, W. Huang and Y. Cui, *Nat. Chem.*, 2019, **11**, 382.
19 A. Kolesnikov, M. Kolek, J. F. Dohmann, F. Horsthemke, M. Börner, P. Bieker, M. Winter and M. C. Stan, *Adv. Energy Mater.*, 2020, **10**, 2070065.
20 C. Wang, A. Wang, L. Ren, X. Guan, D. Wang, A. Dong, C. Zhang, G. Li and J. Luo, *Adv. Funct. Mater.*, 2019, **29**, 1905940.
21 Y. Mu, Y. Chen, B. Wu, Q. Zhang, M. Lin and L. Zeng, *Adv. Sci.*, 2022, **9**, 2203321.
22 Y. Pang, Y. Liu, M. Gao, L. Ouyang, J. Liu, H. Wang, M. Zhu and H. Pan, *Nat. Commun.*, 2014, **5**, 3519.
23 F. Han, L. Fan, X. Ma, H. Lu, L. Li, X. Zhang and L. Wu, *Energy Environ. Mater.*, 2024, **7**, e12623.
24 C. Chen, Y. Kuang, S. Zhu, I. Burgert, T. Keplinger, A. Gong, T. Li, L. Berglund, S. J. Eichhorn and L. Hu, *Nat. Rev. Mater.*, 2020, **5**, 642.
25 J. Wu, J. Li and X. Yao, *Adv. Funct. Mater.*, 2024, 2416671.
26 Y. Zhang, W. Luo, C. Wang, Y. Li, C. Chen, J. Song, J. Dai, E. M. Hitz, S. Xu and C. Yang, *Proc. Natl. Acad. Sci. U. S. A.*, 2017, **114**, 3584.
27 P. Wang, X. Dai, P. Xu, S. Hu, X. Xiong, K. Zou, S. Guo, J. Sun, C. Zhang, Y. Liu, T. Zhou and Y. Chen, *eScience*, 2023, **3**, 100088.
28 C. Zhang, X. Shen, Y. Jin, J. Cheng, C. Cai and F. Wang, *Chem. Rev.*, 2023, **123**, 4510.
29 Y. Sang, H. Chen, M. Khalifeh and Y. Li, *Catal. Today*, 2023, **408**, 168.
30 B. Zhao, X. Shi, S. Khakalo, Y. Meng, A. Miettinen, T. Turpeinen, S. Mi, Z. Sun, A. Khakalo and O. J. Rojas, *Nat. Commun.*, 2023, **14**, 7875.
31 S. Wang, L. Li, L. Zha, S. Koskela, L. A. Berglund and Q. Zhou, *Nat. Commun.*, 2023, **14**, 2827.
32 Y. Ding, Z. Pang, K. Lan, Y. Yao, G. Panzarasa, L. Xu, M. L. Ricco, D. R. Rammer, J. Zhu and M. Hu, *Chem. Rev.*, 2022, **123**, 1843.
33 J. Chen, F. Zhang, M. Kuang, L. Wang, H. Wang, W. Li and J. Yang, *Proc. Natl. Acad. Sci. U. S. A.*, 2024, **121**, e2318853121.
34 Q. Xia, C. Chen, Y. Yao, J. Li, S. He, Y. Zhou, T. Li, X. Pan, Y. Yao and L. Hu, *J. Nat. Sci. Sustainable Technol.*, 2021, **4**, 627.
35 J. Chen, M. Jiang, F. Zhang, L. Wang and J. Yang, *Adv. Mater.*, 2024, **36**, 2401867.
36 T. Li, C. Chen, A. H. Brozena, J. Zhu, L. Xu, C. Driemeier, J. Dai, O. J. Rojas, A. Isogai and L. Wågberg, *Nature*, 2021, **590**, 47.
37 H. He, R. Zhang, P. Zhang, P. Wang, N. Chen, B. Qian, L. Zhang, J. Yu and B. Dai, *Adv. Sci.*, 2023, **10**, 2205557.

38 H. Zhu, W. Luo, P. N. Ciesielski, Z. Fang, J. Zhu, G. Henriksson, M. E. Himmel and L. Hu, *Chem. Rev.*, 2016, **116**, 9305.
39 Y. Liu, J. Xue, T. Zheng and J. Dahn, *Carbon*, 1996, **34**, 193.
40 X. Dai, G. Lv, Z. Wu, X. Wang, Y. Liu, J. Sun, Q. Wang, X. Xiong, Y. Liu, J. Sun, Q. Wang, X. Xiong, Y. Liu, C. Zhang, S. Xin, Y. Chen and T. Zhou, *Adv. Energy Mater.*, 2023, **13**, 2300452.
41 H. Liu, T. Wu, L. Zhang, X. Wang, H. Li, S. Liu, Q. Zhang, X. Zhang and H. Yu, *ACS Nano*, 2022, **16**, 14402.
42 T. Lv, J. Xiao, W. Weng and W. Xiao, *Adv. Energy Mater.*, 2020, **10**, 2002241.
43 K. Zou, T. Zhou, Y. Chen, X. Xiong, W. Jing, X. Dai, M. Shi, N. Li, J. Sun, S. Zhang, C. Zhang, Y. Liu and Z. Guo, *Adv. Energy Mater.*, 2022, **12**, 2103981.
44 H. Song, X. Chen, G. Zheng, X. Yu, S. Jiang, Z. Cui, L. Du and S. Liao, *ACS Appl. Mater.*, 2019, **11**, 18361.
45 M. Baek, J. Kim, K. Jeong, S. Yang, H. Kim, J. Lee, M. Kim, K. J. Kim and J. W. Choi, *Nat. Commun.*, 2023, **14**, 1296.
46 Q. Dong, B. Hong, H. Fan, C. Gao, X. Huang, M. Bai, Y. Zhou and Y. Lai, *Energy Storage Mater.*, 2022, **45**, 1220.
47 B. Acebedo, M. C. Morant-Miñana, E. Gonzalo, I. R. de Larramendi, A. Villaverde, J. Rikarte and L. Fallarino, *Adv. Energy Mater.*, 2023, **13**, 2203744.
48 F. Wang, P. Li, W. Li and D. Wang, *ACS Nano*, 2022, **16**, 7689.
49 H. Li, R. Hua, Y. Xu, D. Ke, C. Yang, Q. Ma, L. Zhang, T. Zhou and C. Zhang, *Chem. Sci.*, 2023, **14**, 10147–10154.
50 S. Xia, Z. Jiang, X. Zhao, J. A. Yuwono, X. Zhang, X. Zhang, G. Yang, J. Yang, Y. Jiang and J. Mao, *Adv. Energy Mater.*, 2024, **14**, 2304407.
51 Y. Zhang, W. Wang, Y. Zhao, X. Zhang, H. Guo, H. Gao, D. Xu, Y. Zhao, G. Li, J. Liang, S. Xin and Y. Guo, *Adv. Funct. Mater.*, 2024, **34**, 2310309.
52 Y. Gao, B. Cui, J. Wang, Z. Sun, Q. Chen, Y. Deng, X. Han and W. Hu, *Rare Met.*, 2022, **41**, 3391–3400.
53 Q. Shen, Y. Liu, X. Zhao, J. Jin, Y. Wang, S. Li, P. Li, X. Qu and L. Jiao, *Adv. Funct. Mater.*, 2021, **31**, 2106923.
54 W. Martin, Y. Tian and J. Xiao, *J. Electrochem. Soc.*, 2021, **168**, 060513.
55 J. Tan, J. Matz, P. Dong, J. Shen and M. Ye, *Adv. Energy Mater.*, 2021, **11**, 2100046.
56 W. Yin, P. Su, Q. Lu, X. Li, J. Peng, T. Zhou, G. Liang, Y. Cao, H. Wang, Q. Li and S. Hu, *Rare Met*, 2024, **43**, 1589–1598.
57 T. Gao, Y. Han, D. Fraggedakis, S. Das, T. Zhou, C.-N. Yeh, S. Xu, W. C. Chueh, J. Li and M. Z. Bazant, *Joule*, 2021, **5**, 393.
58 G. Li, X. Duan, X. Liu, R. Zhan, X. Wang, J. Du, Z. Chen, Y. Li, Z. Cai and Y. Shen, *Adv. Mater.*, 2023, **35**, 2207310.
59 H. Lin, Z. Zhang, Y. Wang, X. L. Zhang, Z. Tie and Z. Jin, *Adv. Funct. Mater.*, 2021, **31**, 2102735.
60 J. Pu, J. Li, K. Zhang, T. Zhang, C. Li, H. Ma, J. Zhu, P. V. Braun, J. Lu and H. Zhang, *Nat. Commun.*, 2019, **10**, 1896.
61 Y. Jin, Q. He, G. Liu, Z. Gu, M. Wu, T. Sun, Z. Zhang, L. Huang and X. Yao, *Adv. Mater.*, 2023, **35**, 2211047.